

Kinetic Inductance of Few-Layer NbSe₂ in the Two-Dimensional Limit

Sameia Zaman^{1,2}, Joel I.-j. Wang^{1*}, Thomas Werkmeister³, Miuko Tanaka¹, Thao Dinh⁴, Max Hays¹, Daniel Rodan-Legrain¹, Aranya Goswami¹, Réouven Assouly¹, Ahmet Kemal Demir⁴, David K. Kim⁵, Bethany M. Niedzielski⁵, Kyle Serniak^{1,5}, Mollie E. Schwartz⁵, Kenji Watanabe⁶, Takashi Taniguchi⁷, Philip Kim^{3,8}, Riccardo Comin⁴, Jeffrey A. Grover¹, Terry P. Orlando^{1,2}, Pablo Jarillo-Herrero⁴, and William D. Oliver^{1,2,4*}

¹Research Laboratory of Electronics, Massachusetts Institute of Technology, Cambridge, MA 02139, USA

²Department of Electrical Engineering and Computer Science, Massachusetts Institute of Technology, Cambridge, MA 02139, USA

³John A. Paulson School of Engineering and Applied Sciences, Harvard University, Cambridge, MA, USA

⁴Department of Physics, Massachusetts Institute of Technology, Cambridge, MA 02139, USA

⁵Lincoln Laboratory, Massachusetts Institute of Technology, Lexington, MA 02421, USA

⁶Research Center for Electronic and Optical Materials, National Institute for Materials Science, 1-1 Namiki, Tsukuba 305-0044, Japan

⁷Research Center for Materials Nanoarchitectonics, National Institute for Materials Science, 1-1 Namiki, Tsukuba 305-0044, Japan

⁸Department of Physics, Harvard University, Cambridge, MA, USA

*To whom correspondence should be addressed: joelwang@mit.edu, and william.oliver@mit.edu

Abstract

Van der Waals (vdW) superconductors remain superconducting down to the monolayer limit, enabling the exploration of emergent physical phenomena and functionality driven by reduced dimensionality. Here, we report the characterization of the kinetic inductance of atomically thin NbSe₂, a two-dimensional van der Waals superconductor, using superconducting coplanar waveguides and microwave measurement techniques familiar to circuit quantum electrodynamics (cQED). The kinetic inductance scales inversely with the number of NbSe₂ layers, reaching 1.2 nH/□ in the monolayer limit. Furthermore, the measured kinetic inductance exhibits a thickness-dependent crossover from clean- to dirty-limit behavior, with enhanced dirty-limit contributions emerging in the ultra-thin regime. These effects are likely driven by increased surface scattering, multi-band superconductivity, and geometric confinement. Additionally, the self-Kerr nonlinearity of the NbSe₂ films ranges from $K/2\pi = -0.008$ to -14.7 Hz/photon, indicating its strong potential in applications requiring compact, nearly linear, high-inductance superconducting quantum devices and detectors. The fabrication and characterization techniques demonstrated here are extensible to the investigation of other two-dimensional superconductors.

Introduction

Kinetic inductance (L_k) in a superconductor arises from the inertia of Cooper pair transport in response to a varying electromagnetic field. Unlike geometric inductance, which varies with the geometry of the electronic element, kinetic inductance depends on intrinsic properties of the material, e.g., superfluid density, carrier effective mass, and film thickness. For example, in a clean superconductor, the kinetic inductance per square is $L_{k,\text{sq}} = m_{\text{eff}}/e^2 n_0 d$, where m_{eff} is the effective mass of the charge carriers, n_0 is the superfluid density (number of Cooper pairs per unit volume) per unit thickness, and d is the thickness of the sample. This relation indicates that $L_{k,\text{sq}}$ increases with decreasing film thickness or suppressed superfluid density. Such an enhancement is useful in quantum circuits, where superconductors with high- L_k are used to realize superinductors — inductive elements with a reactance that approaches and even exceeds the quantum unit $R_Q = h/(2e)^2 = 6.4$ kΩ for Cooper pairs, where h is the Planck constant, and e is the elementary charge. Furthermore, the kinetic inductance in a superconductor is directly related to the superfluid stiffness; probing it enables insight into several fundamental properties such as the superconducting gap structure and pairing symmetry in unconventional superconductors [1–4].

Superconductors are used in a variety of applications, including in superconducting qubit circuits such as fluxonium and $0-\pi$ qubits, which require large (and ideally linear) shunt inductance [5, 6]. They have also been used to realize coherent quantum phase slip circuits [7, 8], long-range coupling for spin qubits [9], and tailored Kerr non-linearities in light-matter interactions [10, 11]. Furthermore, these materials can be used for wide-band parametric amplifiers and high-impedance readout resonators [12–15]. For many of these applications, low- L_k aluminum is used, and thus, large inductance is realized primarily by an array of Al-AlO_x-Al Josephson junctions [16–18]. However, these junctions exhibit strong nonlinearity and are therefore limited in the current they can support while remaining in the linear inductance regime. This motivates the search for alternative materials that can provide large inductance with minimal nonlinearity. Recent efforts toward this goal have focused on implementing superconductors using amorphous superconducting thin films, such as TiN [19, 20], NbN [21, 22], NbTiN [23, 24], InO_x [7, 25], NbSi [26], WSi [27], AlO_x [28], and granular Al [29, 30]. The inherent disorder of these materials suppresses the density of Cooper-pairs, leading to high- L_k in the superconducting regime [31]. Typically, these amorphous superconductors operate in the dirty limit, where the mean free path of charge carriers is shorter than the superconducting coherence length [32]. This relationship implies that, in the BCS framework, the size of a Cooper pair is greater than the average travel distance between consecutive scattering sites. In contrast, the coherence length of a clean superconductor is shorter than its mean free path, and Cooper pair transport can be regarded as ballistic when the length of the device is shorter than the mean free path.

In superconducting quantum devices, disorder and the resulting scattering of charge carriers are expected to affect quasiparticle dynamics and, consequently, device coherence. While the link between disorder, quasiparticle generation, and the associated noise remains an area of active investigation [29, 33–35], microwave characterization of superconductors with varied disorder levels may offer a way to probe their dynamic responses and help explore the role of scattering in decoherence [35].

NbSe₂—a van der Waals Superconductor

We investigate 2H-NbSe₂ (further referred to as NbSe₂ for brevity), a transition-metal dichalcogenide and a type-II superconductor. The lattice structure of NbSe₂ is hexagonal, with the Nb atoms in trigonal prismatic coordination surrounded by Se atoms (Fig. 1a). The layers are stacked in an ABAB sequence along the c-axis and are bonded by van der Waals forces between adjacent layers. NbSe₂ possesses out-of-plane mirror symmetry and broken in-plane inversion symmetry. This broken in-plane symmetry gives rise to an unconventional Ising spin-orbit coupling, which maintains superconductivity in the presence of a strong in-plane magnetic field exceeding 30 T, as observed in the monolayer limit [36, 37]. Both superconductivity

and the charge-density wave transition exist from the bulk down to monolayer thickness. However, the superconducting transition temperature (T_c) decreases with reduced film thickness, attributable to a suppressed Cooper-pair density, the presence of a superconductor–vacuum interface, and modifications to the electronic band structure [38, 39]. As the thickness is reduced, NbSe_2 exhibits several unusual quantum phenomena—including thickness-dependent Higgs modes [40], dissipationless phase diagrams [41], unconventional finite momentum pairing [42–44], and the emergence of a quantum metallic phase under a small perpendicular magnetic field [45]. Prior direct current (DC) transport studies indicate that the carrier mean free path in NbSe_2 decreases with its thickness due to enhanced surface scattering [38, 41]. When encapsulated by hBN, even bilayer and monolayer NbSe_2 exhibit mean free paths (approximately 17 nm and 15 nm, respectively) that are larger than their corresponding superconducting coherence length (8 nm) [37, 38, 42]. These DC transport measurements are consistent with encapsulated NbSe_2 exhibiting superconductivity in the clean limit [38, 46–48].

While previous studies have primarily relied on DC transport to probe only the real part of the conductivity, in this work, we measure the kinetic inductance to access the complex conductivity of few-layer NbSe_2 in the two-dimensional limit. This method allows us to determine whether the material lies in the clean limit, the dirty limit, or an intermediate regime. Moreover, it is sensitive to fundamental superconducting properties such as superfluid stiffness, surface impedance, and loss mechanisms [2, 49, 50], providing insight into the material suitability for superconducting quantum devices operating in the microwave regime.

Device Design

We study the kinetic inductance of hBN-encapsulated NbSe_2 thin films using quarter-wavelength $\lambda/4$ coplanar waveguide (CPW) resonators made of thin-film Al. The resonant frequency of a resonator is $f_r = \frac{1}{2\pi\sqrt{L_{\text{eff}}C_{\text{eff}}}}$, where L_{eff} and C_{eff} are the effective inductance and capacitance of the resonator, respectively (Fig. 1b, left panel). The Al inductance is primarily geometric, and its kinetic inductance per square is much smaller than that of NbSe_2 . When the $\lambda/4$ -resonator is terminated to ground by an NbSe_2 sample, the resonant frequency shifts to a lower frequency $f_{r'} = \frac{1}{2\pi\sqrt{L'_{\text{eff}}C'_{\text{eff}}}}$ due to the additional kinetic inductance from the NbSe_2 (Fig. 1b, right panel). We perform microwave simulations to determine the expected frequency shift of a $\lambda/4$ -resonator due to the additional inductance L_k (Fig. 1c). The Al-only resonator has a frequency of 5.6 GHz. When terminated by NbSe_2 , the resonance frequency decreases by 200 MHz per 0.1 nH of added termination inductance.

Figure 2a shows an optical micrograph of the superconducting circuit with $\lambda/4$ CPW resonators used for

this work. The aluminum CPW resonators are fabricated from a 250 nm Al film deposited on a high-resistivity silicon substrate and patterned using a combination of photolithography and wet etching (see Ref. [2] and Supplementary Information for details). Two $\lambda/4$ -resonators, an aluminum *spectator* resonator and an *experiment* resonator, are capacitively coupled to a common feedline. The spectator resonator is used as a witness to monitor the impact of the vdW materials fabrication process (without incorporating vdW materials), while the experiment resonator is terminated by a NbSe_2 sample situated within a square hosting window of size 200 μm by 200 μm . To extract the kinetic inductance of each NbSe_2 device, we analyze two $\lambda/4$ -resonators: the NbSe_2 -terminated experiment resonator (Fig. 2b) and a control resonator of the same geometry that is terminated instead by a 250 nm-thick aluminum film (Fig. 2c). The NbSe_2 thin film is encapsulated in hBN to maintain a nominally clean and atomically flat interface while ensuring a relatively low-microwave-loss environment [50, 51]. This hBN- NbSe_2 -hBN heterostructure is assembled through mechanical exfoliation and standard dry-transfer techniques inside an argon-filled glove box, ensuring minimal oxidation of the NbSe_2 before full encapsulation.

The hBN- NbSe_2 -hBN heterostructure is galvanically connected to the microwave resonator and the ground plane. To achieve a highly transparent, superconducting contact, we make a one-dimensional edge-contact to the NbSe_2 using reactive ion etching of the heterostructure, followed by in-situ argon ion milling and aluminum deposition (Fig. 2d) [52]. A low-loss superconducting contact is critical to maintaining a narrow resonance line (i.e., a high quality factor of the resonator), which translates to higher measurement resolution of the resonator frequency. Details of the fabrication process and the verification of the superconducting contact are provided in the Supplementary Information.

Microwave Characterization of NbSe_2

The samples are characterized in a dilution refrigerator with a base temperature of approximately 10 mK (see Fig. S2 for wiring diagram). The microwave transmission coefficient S_{21} is measured as a function of frequency using a two-port vector network analyzer (VNA). Figure 3a shows a representative $|S_{21}|$ measurement from a $\lambda/4$ -resonator terminated by a 9-nm-thick (determined by AFM) NbSe_2 film (Device ID D6). The resonant frequency $f_{\text{r},\text{Al}-\text{NbSe}_2}$ and quality factor are determined from a Lorentzian fit using the standard circular fit procedure [53] (Fig. 3a inset and Supplementary Information). In the single-photon limit, the NbSe_2 -terminated resonator exhibits a resonant frequency $f_{\text{r},\text{Al}-\text{NbSe}_2} = 4.79 \text{ GHz}$ and an internal quality factor $Q_{\text{i},\text{Al}-\text{NbSe}_2} = 2.8 \times 10^4$, while the Al-terminated control resonator has a resonant frequency $f_{\text{r},\text{Al}} = 5.34 \text{ GHz}$ and an internal quality factor $Q_{\text{i},\text{Al}} = 1.0 \times 10^5$. The lower internal quality factor observed in the NbSe_2 -terminated Al resonator is likely due to additional dissipation arising from imperfect electrical contacts

between the Al and the NbSe_2 , as well as dielectric loss introduced by residual polymer contamination from the dry transfer process. Moreover, the frequency difference $f_{\text{r,Al}} - f_{\text{r,Al-NbSe}_2} = 0.45 \text{ GHz}$ highlights the impact of terminating the resonator with NbSe_2 and enables us to extract a kinetic inductance $L_{\text{k,sq}} = 124 \text{ pH}$ for this NbSe_2 sample.

The resonant frequency of the NbSe_2 -terminated resonator decreases with increasing microwave probe power, e.g., with a noticeable downshift in $f_{\text{r,Al-NbSe}_2}$ at the estimated sample power of -90 dBm (Fig. 3b, green arrow). This frequency downshift indicates a contribution from kinetic inductance. As the microwave power increases, enhanced Cooper-pair breaking leads to a reduction in the superfluid density (n_0), resulting in a larger kinetic inductance L_{k} and, consequently, a lower resonant frequency. In contrast, the aluminum resonator exhibits no observable power dependence up to an estimated input power of -60 dBm at the sample (Fig. S4b), corresponding to the upper limit of our VNA output (VNA outputs a power of 10 dBm at room temperature, which is reduced to -60 dBm at the sample after passing through a total attenuation of 70 dB), confirming that its inductance is predominantly geometric. The nonlinear microwave power dependence exhibited by the NbSe_2 -terminated resonator, observed over the power range from -100 dBm to -80 dBm , is well-described by a Kerr-type or Duffing-type nonlinearity [54] (see Supplementary Information). When the microwave power in the resonator exceeds a critical threshold, the resonant frequency bifurcates and enters a bistability regime (Fig. 3b, blue arrow) [55–57]. From a linear fit of the resonant frequency shift ($\Delta f = f_{\text{r,Al-NbSe}_2}(n_{\text{r}} = 1) - f_{\text{r,Al-NbSe}_2}(n_{\text{r}})$) with the photon number of the resonator (n_{r}), shown in Fig. 3c, we extract a self-Kerr coefficient $K/2\pi = -1.7 \text{ Hz/photon}$ at 10 mK . Typically, conventional superconducting inductors of similar dimensions, such as granular aluminum, with a self-Kerr coefficient of 4.5 MHz [58], and Josephson junction arrays, with a self-Kerr of 8 MHz [59]—exhibit significantly higher nonlinearity. In contrast, NbSe_2 films show a lower self-Kerr coefficient, indicating low nonlinearity.

We also investigate the dependence of the kinetic inductance on the DC bias current. A DC bias current I_{DC} is introduced via a contact to the microwave line just above the NbSe_2 termination (Fig. 3d), while a microwave tone is maintained in the low-power linear regime ($P_{\text{rf}} = -120 \text{ dBm}$). The resonant frequency ($f_{\text{r,Al-NbSe}_2}$) decreases with an increasing bias current (up to $I_{\text{DC}} = 30 \mu\text{A}$), indicating a corresponding increase in kinetic inductance (Fig. 3e). This behavior is similar to the microwave response due to the Kerr-type nonlinearity. In the Ginzburg-Landau framework, the dependence of kinetic inductance of the superconducting film with bias current is well-described by a quadratic function (ignoring the terms beyond

2nd order) [32]:

$$L_k(I_{\text{DC}}) = L_k(0) \left[1 + \left(\frac{I_{\text{DC}}}{I^*} \right)^2 + \dots \right], \quad (1)$$

where $L_k(0)$ is the kinetic inductance of the resonator at zero current bias, and I^* is a characteristic current, also known as the depairing current. I^* is typically comparable to the superconducting critical current I_c , and sets the scale of non-linearity. By fitting to this relationship, I^* is determined to be 0.4 mA for the 9 nm thick, 3.9 μm wide NbSe₂ sample. We observe that both the resonant frequency and the kinetic inductance per square exhibit a quadratic dependence on the DC bias current (Fig. 3f), consistent with the anisotropic nodeless pairing of NbSe₂ reported in previous studies [43, 60].

Layer Dependence of L_k in NbSe₂

VdW superconductors remain superconducting in the monolayer limit [36, 61], which enables one to increase kinetic inductance by reducing the thickness. Figure 4a shows the sheet kinetic inductance ($L_{k,\text{sq}}$) of NbSe₂ films extracted from microwave measurements as a function of thickness (d) and the corresponding layer numbers. The measured $L_{k,\text{sq}}$ (red circles) exhibits an approximate $1/d$ dependence, as expected for thin superconducting films, and reaches 1.2 nH for the monolayer sample (see Supplementary Information for the determination of layer numbers). The values are compared to those of other superconductors based on amorphous materials, including TiN[19, 62], NbTiN[23, 24], granular aluminum (gr-Al)[58], and NbN[21] across a range of film thicknesses up to 13 nm, as shown in Fig. 4b. Notably, NbSe₂, particularly in the few-monolayer regime, exhibits one of the highest sheet kinetic inductances reported at comparable thicknesses, surpassing those of many conventional high-impedance superconductors.

The observed layer dependence may provide insight into the underlying mechanisms responsible for the high L_k , including the role of scattering processes, and whether our NbSe₂ devices operate in the dirty limit, the clean limit, or an intermediate regime. We consider a general expression for the sheet kinetic inductance $L_{k,\text{sq}}$ that spans from the clean to the dirty limit (see Supplementary Information for the derivation):

$$L_{k,\text{sq}} = \frac{1}{d} \left(\frac{m_{\text{eff}}}{n_0 e^2} + \frac{\hbar}{1.764 k_B T_c} \rho_s \right) = \frac{m_{\text{eff}}}{n_0 e^2 d} + \frac{\hbar}{1.764 k_B T_c} R_s \quad (2)$$

Here, ρ_s denotes the normal-state sheet resistivity, \hbar is the reduced Planck's constant, k_B is the Boltzmann constant, and R_s is the normal-state sheet resistance. If we assume that the term in parentheses varies slowly with film thickness, then we expect the approximate $1/d$ dependence that we see in Fig. 4a. This expression suggests that the total kinetic inductance arises from a combination of clean-limit (first term)

and dirty-limit (second term) contributions. Figure 4c plots the measured sheet kinetic inductance $L_{k,\text{sq}}$ as a function of R_s/T_c . The R_s and T_c values are obtained from both our transport measurements and previous studies (shown in green and black circles in Fig. 4c, summarized in Table S3). We observe a linear dependence for the larger values of $L_{k,\text{sq}}$ in Fig. 4c. A linear fit yields a slope of 16.3 which characterizes the dirty-limit dependence, and the y-intercept of 80.0 pH shows that there is a significant contribution from the clean-limit for thicker samples (note that the $1/d$ dependence for the clean-limit term can be considered, but qualitatively, the contribution from the clean-limit term remains significant). As the sample thickness approaches the monolayer limit, the ratio of the measured kinetic inductance to the clean-limit kinetic inductance ($L_{k,\text{sq}}/L_{k,\text{sq},\text{clean}}$) increases from 0.7 to 15 monotonically, indicating that the dirty-limit contribution becomes increasingly significant in thinner NbSe₂ samples. This model captures the crossover from clean to the dirty-limit behavior as the sample thickness decreases.

We now discuss possible origins of the observed crossover behavior. In thicker NbSe₂ films, the majority of charge carriers reside in the interior layers of the 2D crystal. The clean-limit-like behavior observed in this regime—corresponding to the lower-left corner of Fig. 4c—may be attributed to the high crystallinity of the bulk material and effective screening from carriers in the top and bottom NbSe₂ layers. In contrast, thinner devices exhibit a greater influence from their surrounding environment. In the monolayer limit, all charge carriers are in close proximity to the encapsulating hBN on both sides, leading to enhanced surface scattering from impurities or fabrication residues. This increased scattering may result in more pronounced dirty-limit contributions to the kinetic inductance. Moreover, NbSe₂ has been shown to host two superconducting bands with distinct gap sizes, with the larger gap decreasing monotonically as thickness is reduced [60]. In other multi-band superconductors [63, 64], such disparity across the Fermi surface has been linked to the coexistence of clean- and dirty-limit behaviors, arising from band-dependent coherence lengths and scattering rates. Our experiment does not explicitly resolve contributions from individual bands, but similar multi-band effects may contribute to the observed layer dependence of kinetic inductance in NbSe₂ (Fig. 4c). Additionally, as the superconducting gap (or T_c) decreases with reduced thickness, the superconducting coherence length becomes longer. For a fixed mean free path, this leads to a larger coherence length to mean free path ratio, indicating a shift toward dirty-limit behavior in the thinner samples. We note that the combined contributions from both clean- and dirty-limit superconductivity observed in the microwave measurements here contrast with previous DC transport studies, which reported only clean-limit behavior. This discrepancy suggests that the microwave response may be sensitive to the multi-band nature of NbSe₂ [38, 46–48].

Finally, in thin superconducting films where the thickness d is much smaller than the penetration depth λ ,

the relevant length scale becomes the Pearl length $\Lambda = \frac{2\lambda^2}{d}$ [65]. All of our NbSe_2 samples operate in this Pearl regime ($d \ll \lambda \sim 230 \text{ nm}$ [66]), with both thickness and width much smaller than the estimated Pearl length (10-70 μm ; see Supplementary Information). Recent studies on high- T_c YBCO superconductors have shown that geometric confinement in this regime can strongly enhance the kinetic inductance as the device width approaches or falls below Λ [67]. While a detailed investigation of this effect in NbSe_2 lies beyond the scope of this work, our observation of large L_k values — and a steeper-than-expected inverse thickness scaling, relative to the prediction of Eq. 2 — may be qualitatively consistent with such confinement-enhanced kinetic inductance in the Pearl regime.

Conclusions

We characterize the kinetic inductance and nonlinear properties of NbSe_2 using a coplanar waveguide resonator terminated by hBN-encapsulated NbSe_2 thin films. The kinetic inductance shows an approximate $1/d$ -type scaling for the thinner samples and reaches $1.2 \text{ nH}/\square$ at monolayer thickness — among the highest reported for superconductors within this thickness regime. Under the microwave drive, the device exhibits a nonlinear frequency shift that is consistent with the nonlinear Kerr model. The extracted Kerr coefficients ($K/2\pi = -0.008$ to $14.7 \text{ Hz}/\text{photon}$) are relatively small, making NbSe_2 well-suited for applications that require large linear inductance with minimal nonlinearity, such as the linear shunt-inductor used in fluxonium qubits and in photon detectors operating in the microwave regime [68]. The L_k exhibits a quadratic dependence on DC bias current, consistent with the Ginzburg-Landau framework.

The measured kinetic inductance in NbSe_2 exhibits a crossover from clean- to dirty-limit behavior as the thickness decreases. This transition can be qualitatively described using a generalized expression for L_k derived from BCS theory. In the ultra-thin regime, enhanced contributions from the dirty limit may arise due to increased surface scattering, multi-band superconductivity, and geometric confinement.

We demonstrate that NbSe_2 is a crystalline two-dimensional superconductor that exhibits large, linear inductance. The hBN- NbSe_2 -hBN heterostructure is well suited for compact lump-element devices, such as shunt inductors for fluxonium qubits or readout resonators, while minimizing parasitic coupling. These results also highlight the ability of microwave measurements to probe superconducting properties in low-dimensional materials, offering a valuable complement to DC transport and other techniques.

Acknowledgements

The authors thank Shoumik D. Chowdhury, Aziza Almanakly, Lamia Ateshian, David Rower, Xirui Wang, Xueqiao Wang, and the device packaging team at MIT Lincoln Laboratory for their assistance in measurement, fabrication, and packaging. This work was carried out in part using the MIT.nano's facilities. This research was funded in part by the US Army Research Office grant no. W911NF-22-1-0023, by the National Science Foundation grant no. 2412810 and no. OMA-1936263, by the Air Force Office of Scientific Research grant no. FA2386-21-1-4058, and under Air Force Contract No. FA8702-15-D-0001. S.Z. acknowledges support from the Lisa Su (1990) Fellowship awarded by the EECS Department at MIT as well as the Faculty for the Future Fellowship from the Schlumberger Foundation. T. W. and P. K. acknowledge support from DOE contract DE-SC0012260. M.H. is supported by an appointment to the Intelligence Community Postdoctoral Research Fellowship Program at the Massachusetts Institute of Technology, administered by Oak Ridge Institute for Science and Education (ORISE) through an interagency agreement between the U.S. Department of Energy and the Office of the Director of National Intelligence (ODNI). D. R-L. acknowledges support from the Rafael del Pino Foundation. R.C. and A.K.D acknowledge support from the U.S. Department of Energy, Office of Science National Quantum Information Science Research Center's Co-design Center for Quantum Advantage (C2QA) under contract number DE-SC0012704. K.W. and T.T. acknowledge support from the JSPS KAKENHI (Grant Numbers 21H05233 and 23H02052), the CREST (JPMJCR24A5), JST, and the World Premier International Research Center Initiative (WPI), MEXT, Japan. P.J-H. acknowledges support by the National Science Foundation (DMR-1809802), the Gordon and Betty Moore Foundation's EPiQS Initiative through Grant No. GBMF9463, the Fundacion Ramon Areces, and the CIFAR Quantum Materials program. Any opinions, findings, conclusions, or recommendations expressed in this material are those of the author(s) and do not necessarily reflect the views of the U.S. Air Force or the U.S. Government.

Author Contributions

J.Î-j.W. conceived and designed the experiment. S.Z., J.Î-j.W., and T.H.D. performed the microwave simulations. S.Z., T. W., M.T., J.Î-j.W., D. R-L., A.G., A.K.D., D.K.K., and B.M.N. contributed to the device fabrication and characterization. S.Z., J.Î-j.W., T. W., R. A., M. H., and D. R-L participated in the measurements. S.Z., J.Î-j.W., R. A., and M.H. analyzed the data. K.W. and T.T. grew the hBN crystal. S.Z., J.Î-j.W., and W.D.O. led the paper writing, and all other authors contributed to the text. J.Î-j.W., J.A.G., K.S. M.E.S., R.C., P.K., P.J-H., T.P.O, and W.D.O supervised the project.

Competing Interests Statement

The authors declare no competing interests.

Device ID	d (nm)	W (μm)	L (μm)	$f_{r,\text{Al-NbSe}_2}$ (GHz)	$f_{r,\text{Al}}$ (GHz)	L_k (nH)	$L_{k,\text{sq}}$ (nH/sq)	$Q_{i,\text{Al-NbSe}_2}$	$K/2\pi$ (Hz)
D1	1.99	3.1	3.1	3.62	5.30	1.195	1.195	0.8×10^4	-14.7
D2	4.08	2.5	5.7	4.14	5.21	0.643	0.282	6.0×10^4	-3.8
D3	5.86	2.6	3.0	4.88	5.33	0.220	0.191	0.7×10^4	-2.9
D4	7.13	4.8	6.7	4.93	5.35	0.200	0.143	2.4×10^4	-2.6
D5	7.98	4.5	12.0	4.63	5.33	0.360	0.135	1.2×10^4	-1.9
D6	8.81	3.9	8.6	4.79	5.34	0.274	0.124	2.8×10^4	-1.7
D7	8.90	4.5	4.2	5.26	5.49	0.100	0.107	2.1×10^4	-1.5
D8	10.07	2.5	6.6	5.16	5.49	0.149	0.056	0.7×10^4	-0.4
D9	11.89	6.0	6.9	5.46	5.60	0.057	0.049	0.6×10^4	-0.03
D10	24.73	4.1	7.5	5.34	5.37	0.014	0.008	18×10^4	-0.006
D11	30.20	3.4	6.1	5.42	5.44	0.009	0.005	2.5×10^4	-0.006
D12	52.12	2.3	4.6	5.6	5.62	0.008	0.004	5.8×10^4	-0.008

Table 1: **Summary of kinetic microwave characterization of NbSe_2 samples across different thicknesses.** W and L represent the nominal width and nominal length of the NbSe_2 samples with a thickness of d. $Q_{i,\text{Al-NbSe}_2}$ and Kerr coefficients ($K/2\pi$) are extracted from NbSe_2 -terminated Al resonators. The film thickness (d) is measured with atomic force microscopy (AFM).

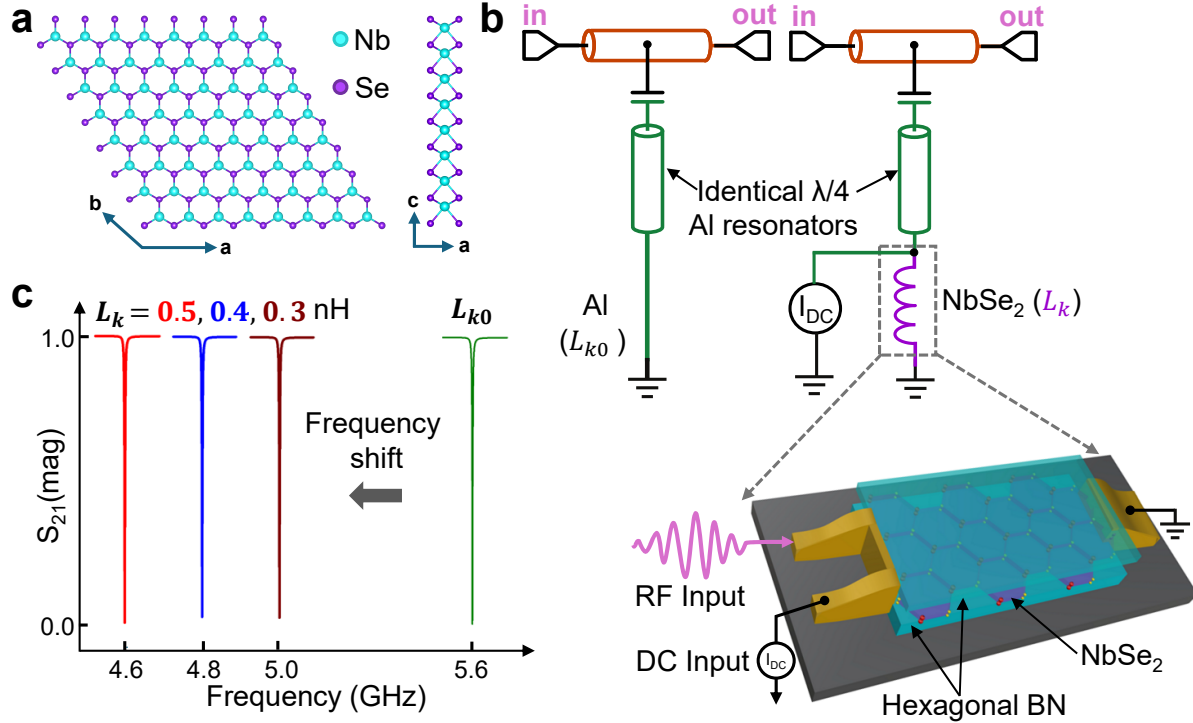


Figure 1: **Superconducting resonators and terminations to characterize the kinetic inductance of NbSe₂.** **a**, Crystal structure of monolayer 2H-NbSe₂, top-down and side views. **b**, Measurement circuit schematic. CPW resonators are capacitively coupled to a common transmission line and terminated either directly to ground via aluminum (control) or through a hBN-NbSe₂-hBN heterostructure (experiment). The resonant frequency f_r of the aluminum $\lambda/4$ resonator is determined by the effective inductance and capacitance of the CPW. Termination by NbSe₂ introduces additional kinetic inductance, shifting the resonant frequency to a new value f_r' . (Zoom-in of inductor) hBN-NbSe₂-hBN heterostructure contacted by Al electrodes with both RF and DC input signals applied across the sample and terminated at ground. **c**, Simulated resonator spectra illustrating the effect of increased inductance on the resonant frequency. L_{k0} denotes the inductance of the aluminum-terminated resonator, while L_k represents the additional inductance introduced by the NbSe₂ sample.

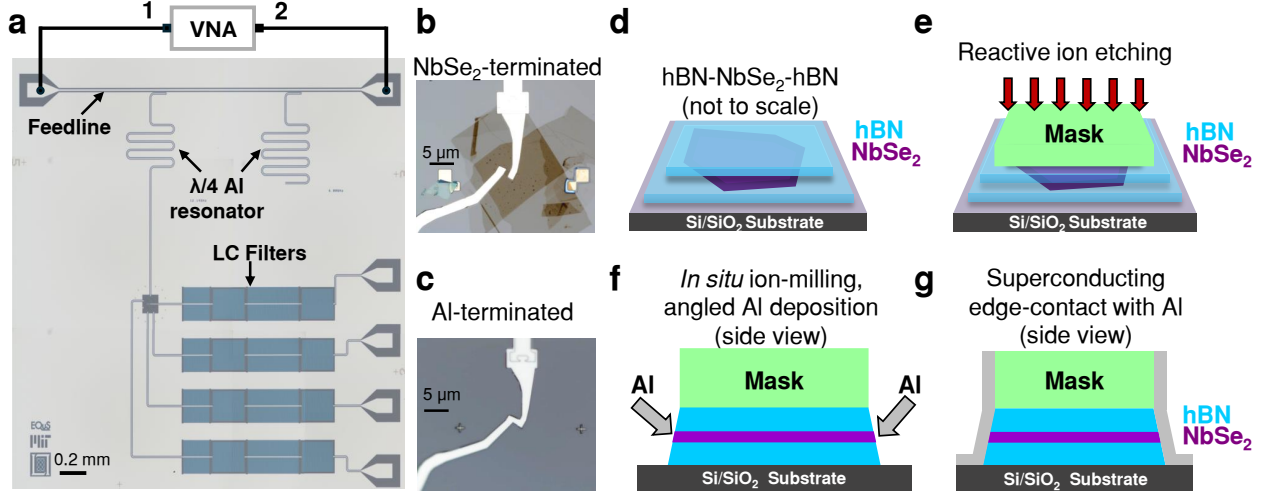


Figure 2: **Measurement configuration and device fabrication for the kinetic inductance measurement of NbSe_2 .** **a**, Optical micrograph of a $5 \times 5 \text{ mm}^2$ chip containing CPW resonators, a shared feedline, DC bias lines, on-chip LC filters, and a ground plane, all patterned from 250 nm-thick aluminum on a high-resistivity silicon substrate. Only one (of four) DC bias lines is used in this experiment. **b - c**, Optical micrographs of the NbSe_2 -terminated and aluminum-terminated $\lambda/4$ CPW resonators, respectively. **d - g**, Illustration of the edge-contact fabrication process. The NbSe_2 (purple) flake is fully encapsulated by hBN (blue) and patterned via reactive-ion etching (RIE) to expose its edges. After in-situ argon ion milling, superconducting edge contacts are formed by angled aluminum evaporation with substrate rotation.

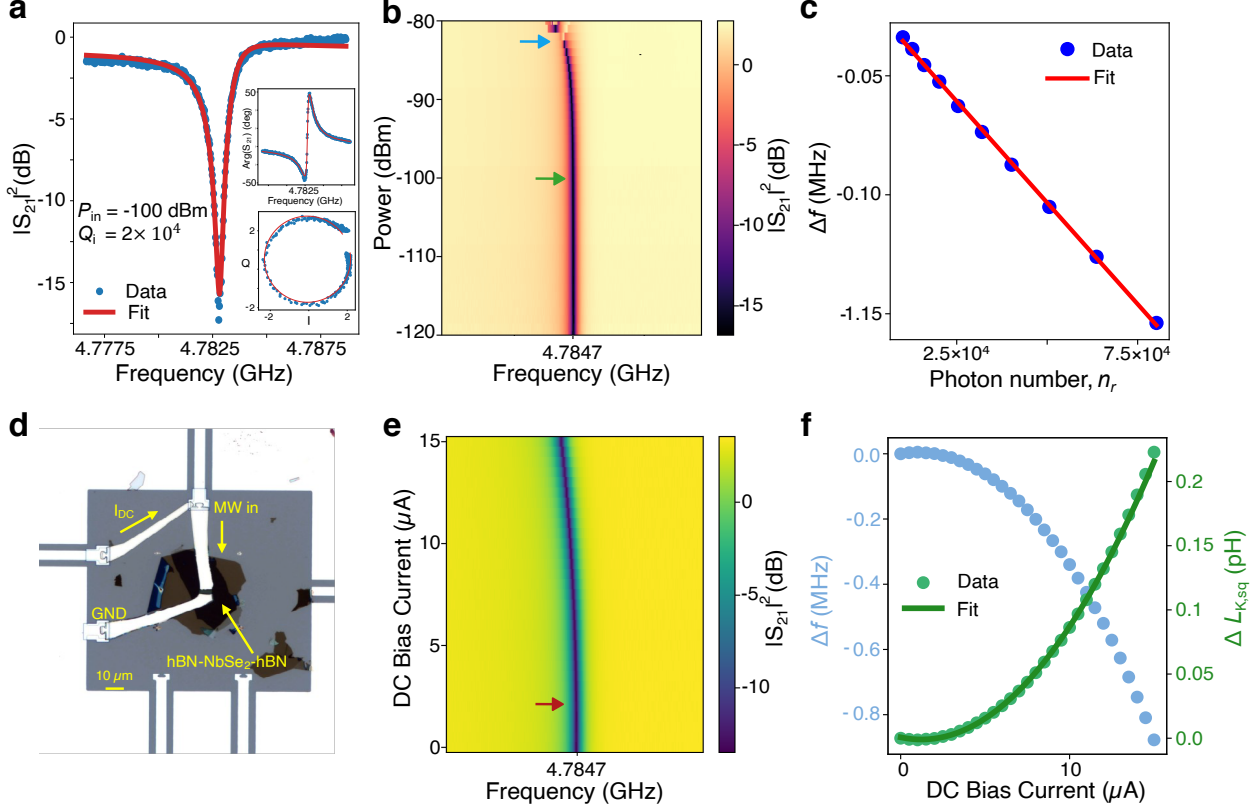


Figure 3: Microwave measurements of NbSe₂-terminated $\lambda/4$ -resonator. **a**, Transmission coefficient ($|S_{21}|$) of a NbSe₂-terminated $\lambda/4$ -resonator measured at 10 mK (Device ID D6). Inset: Complex I-Q plane showing the measured response (blue) and Lorentzian fit (red). **b**, Transmission coefficient ($|S_{21}|$) of NbSe₂-terminated $\lambda/4$ -resonator resonator as a function of input microwave power (P_{rf}). The resonant frequency ($f_{r,Al-NbSe_2}$) shifts to the lower frequency with increasing microwave power. The onset of the frequency shift—defined as exceeding one standard deviation from the low-power baseline ($f_{r,Al-NbSe_2} = 4.785$ GHz)—is observed at an input power of -100 dBm (indicated by the green arrow). At -82 dBm, the resonant peak bifurcates (blue arrow), indicating the onset of a bistable regime. **c**, Linear fit of the resonant frequency shift ($\Delta f = f_{r,Al-NbSe_2}(n_r = 1) - f_{r,Al-NbSe_2}(n_r)$) as a function of resonator photon number (n_r) in the NbSe₂-terminated $\lambda/4$ -resonator. **d**, Optical image of the NbSe₂-terminated $\lambda/4$ -resonator with a DC bias line connected at the microwave input port. **e**, DC bias dependence of the NbSe₂-terminated $\lambda/4$ -resonator measured at a fixed microwave power of $P_{rf} = -120$ dBm. The resonant frequency shifts to the lower frequency with increasing bias current. The onset of the frequency shift—defined as exceeding one standard deviation from the baseline ($f_{r,Al-NbSe_2} = 4.785$ GHz)—is observed at a bias current of $1\ \mu\text{A}$ (maroon arrow). **f**, Extracted resonant frequency shift ($\Delta f = f_{r,Al-NbSe_2}(I_{DC} = 0) - f_{r,Al-NbSe_2}(I_{DC})$) and kinetic inductance shift ($\Delta L_{k,sq} = L_{k,sq}(I_{DC} = 0) - L_{k,sq}(I_{DC})$) of the NbSe₂-terminated resonator as a function of DC bias current. Measured data (circle-green and sky-blue) and theoretical fit (line-green) are shown.

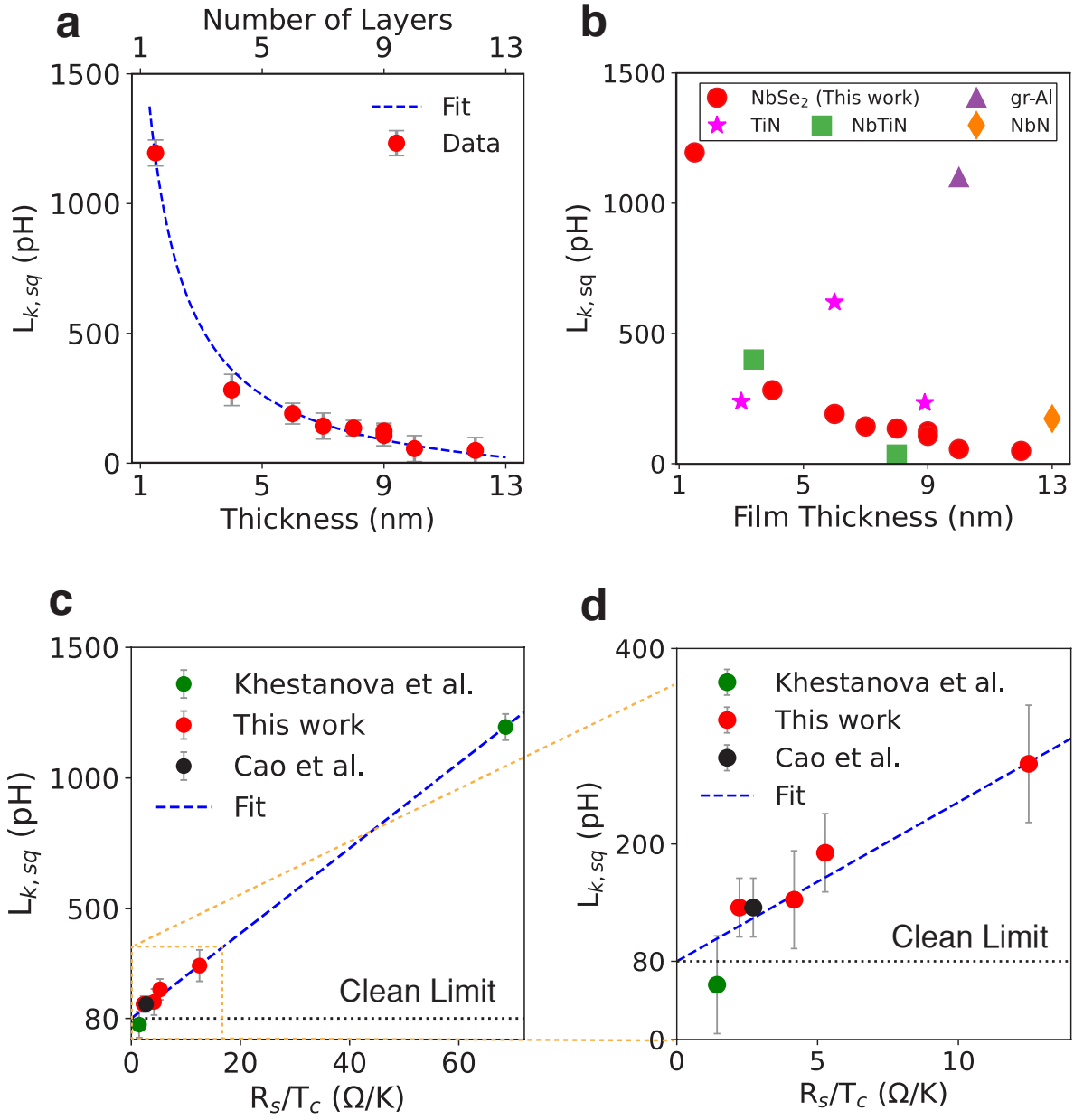


Figure 4: **Thickness dependence of kinetic inductance in NbSe₂.** **a**, Sheet kinetic inductance ($L_{k,sq}$) from microwave measurements (circle-red) of nine NbSe₂ devices with varying film thicknesses. The blue dashed line shows a $1/d$ scaling fit. **b**, Comparison of measured $L_{k,sq}$ in NbSe₂ with values reported for other high-impedance superconducting thin films [19, 21, 23, 24, 58, 62]. **c** Sheet kinetic inductance ($L_{k,sq}$) from microwave measurements is plotted as a function of R_s/T_c , where R_s and T_c values are obtained from both our transport measurements (red circles) and previous studies (green and black circles)[38, 39]. The blue dashed line is a linear fit with a slope of 16.3 and a y-intercept of 80.0 pH, marked as the clean-limit contribution to $L_{k,sq}$. **d**, The magnified view of the lower region for clarity.

References

1. Böttcher, C. *et al.* Circuit quantum electrodynamics detection of induced two-fold anisotropic pairing in a hybrid superconductor–ferromagnet bilayer. *Nature Physics* **20**, 1609–1615 (2024).
2. Tanaka, M. *et al.* Superfluid stiffness of magic-angle twisted bilayer graphene. *Nature* **638**, 99–105 (2025).
3. Banerjee, A. *et al.* Superfluid stiffness of twisted trilayer graphene superconductors. *Nature* **638**, 93–98 (2025).
4. Jin, H. *et al.* Exploring van der Waals cuprate superconductors using a hybrid microwave circuit. *Nano Letters* **25**, 3191–3198 (2025).
5. Manucharyan, V. E., Koch, J., Glazman, L. I., Devoret, M. H., *et al.* Fluxonium: Single cooper-pair circuit free of charge offsets. *Science* **326**, 113–116 (2009).
6. Gyenis, A. *et al.* Experimental realization of a protected superconducting circuit derived from the $0-\pi$ qubit. *PRX Quantum* **2**, 010339 (2021).
7. Astafiev, O. *et al.* Coherent quantum phase slip. *Nature* **484**, 355–358 (2012).
8. Shaikhaidarov, R. S. *et al.* Quantized current steps due to the ac coherent quantum phase-slip effect. *Nature* **608**, 45–49 (2022).
9. Mi, X. *et al.* A coherent spin–photon interface in silicon. *Nature* **555**, 599–603 (2018).
10. Ye, Y. *et al.* Near-ultrastrong nonlinear light-matter coupling in superconducting circuits. *Nature Communications* **16**, 3799 (2025).
11. Puertas Martínez, J. *et al.* A tunable Josephson platform to explore many-body quantum optics in circuit-QED. *npj Quantum Information* **5**, 19 (2019).
12. Böttcher, C. *et al.* Parametric longitudinal coupling between a high-impedance superconducting resonator and a semiconductor quantum dot singlet-triplet spin qubit. *Nature Communications* **13**, 4773 (2022).
13. Clerk, A., Lehnert, K., Bertet, P., Petta, J., Nakamura, Y., *et al.* Hybrid quantum systems with circuit quantum electrodynamics. *Nature Physics* **16**, 257–267 (2020).
14. Landig, A. J. *et al.* Coherent spin–photon coupling using a resonant exchange qubit. *Nature* **560**, 179–184 (2018).
15. Mantegazzini, F. *et al.* High kinetic inductance NbTiN films for quantum limited travelling wave parametric amplifiers. *Physica Scripta* **98**, 125921 (2023).
16. Macklin, C. *et al.* A near–quantum-limited Josephson traveling-wave parametric amplifier. *Science* **350**, 307–310 (2015).

17. Nguyen, L. B. *et al.* High-coherence fluxonium qubit. *Physical Review X* **9**, 041041 (2019).
18. Crescini, N. *et al.* Evidence of dual Shapiro steps in a Josephson junction array. *Nature Physics* **19**, 851–856 (2023).
19. Shearow, A. *et al.* Atomic layer deposition of titanium nitride for quantum circuits. *Applied Physics Letters* **113** (2018).
20. Amin, K. R. *et al.* Loss mechanisms in TiN high impedance superconducting microwave circuits. *Applied Physics Letters* **120** (2022).
21. Frasca, S. *et al.* NbN films with high kinetic inductance for high-quality compact superconducting resonators. *Physical Review Applied* **20**, 044021 (2023).
22. Niegce, D., Burnett, J., Bylander, J., *et al.* High kinetic inductance NbN nanowire superconductors. *Physical Review Applied* **11**, 044014 (2019).
23. Samkharadze, N. *et al.* High-kinetic-inductance superconducting nanowire resonators for circuit QED in a magnetic field. *Physical Review Applied* **5**, 044004 (2016).
24. Bretz-Sullivan, T. M. *et al.* High kinetic inductance NbTiN superconducting transmission line resonators in the very thin film limit. *Applied Physics Letters* **121** (2022).
25. Dupré, O. *et al.* Tunable sub-gap radiation detection with superconducting resonators. *Superconductor Science and Technology* **30**, 045007 (2017).
26. Calvo, M. *et al.* Niobium silicon alloys for kinetic inductance detectors. *Journal of Low Temperature Physics* **176**, 518–523 (2014).
27. Kirsh, N. *et al.* Linear and nonlinear properties of a compact high-kinetic-inductance WSi multimode resonator. *Physical Review Applied* **16**, 044017 (2021).
28. Zhang, W. *et al.* Microresonators fabricated from high-kinetic-inductance aluminum films. *Physical Review Applied* **11**, 011003 (2019).
29. Grünhaupt, L. *et al.* Loss mechanisms and quasiparticle dynamics in superconducting microwave resonators made of thin-film granular aluminum. *Physical Review Letters* **121**, 117001 (2018).
30. Glezer Moshe, A., Farber, E., Deutscher, G., *et al.* Granular superconductors for high kinetic inductance and low loss quantum devices. *Applied Physics Letters* **117** (2020).
31. Charpentier, T. *et al.* First-order quantum breakdown of superconductivity in an amorphous superconductor. *Nature Physics* **21**, 104–109 (2025).
32. Tinkham, M. *Introduction to superconductivity* (Courier Corporation, 2004).
33. Müller, C., Cole, J. H., Lisenfeld, J., *et al.* Towards understanding two-level-systems in amorphous solids: insights from quantum circuits. *Reports on Progress in Physics* **82**, 124501 (2019).

34. Arute, F. *et al.* Quantum supremacy using a programmable superconducting processor. *Nature* **574**, 505–510 (2019).
35. Kurilovich, V. D. *et al.* Correlated Error Bursts in a Gap-Engineered Superconducting Qubit Array. *arXiv preprint arXiv:2506.18228* (2025).
36. Xi, X. *et al.* Ising pairing in superconducting NbSe₂ atomic layers. *Nature Physics* **12**, 139–143 (2016).
37. De la Barrera, S. C. *et al.* Tuning Ising superconductivity with layer and spin-orbit coupling in two-dimensional transition-metal dichalcogenides. *Nature Communications* **9**, 1427 (2018).
38. Khestanova, E. *et al.* Unusual suppression of the superconducting energy gap and critical temperature in atomically thin NbSe₂. *Nano Letters* **18**, 2623–2629 (2018).
39. Cao, Y. *et al.* Quality heterostructures from two-dimensional crystals unstable in air by their assembly in inert atmosphere. *Nano Letters* **15**, 4914–4921 (2015).
40. Du, Y. *et al.* Unveiling resilient superconducting fluctuations in atomically thin NbSe₂ through Higgs mode spectroscopy. *Physical Review Letters* **134**, 066002 (2025).
41. Benyamini, A. *et al.* Fragility of the dissipationless state in clean two-dimensional superconductors. *Nature Physics* **15**, 947–953 (2019).
42. Wan, P. *et al.* Orbital fulde–Ferrell–Larkin–ovchinnikov state in an ising superconductor. *Nature* **619**, 46–51 (2023).
43. Hamill, A. *et al.* Two-fold symmetric superconductivity in few-layer NbSe₂. *Nature physics* **17**, 949–954 (2021).
44. Cho, C.-w. *et al.* Nodal and nematic superconducting phases in NbSe₂ monolayers from competing superconducting channels. *Physical Review Letters* **129**, 087002 (2022).
45. Tsen, A. *et al.* Nature of the quantum metal in a two-dimensional crystalline superconductor. *Nature Physics* **12**, 208–212 (2016).
46. Prober, D., Schwall, R., Beasley, M., *et al.* Upper critical fields and reduced dimensionality of the superconducting layered compounds. *Physical Review B* **21**, 2717 (1980).
47. Zhu, T. *et al.* Transport properties of few-layer NbSe₂: From electronic structure to thermoelectric properties. *Materials Today Physics* **27**, 100789 (2022).
48. Benyamini, A. *et al.* Blockade of vortex flow by thermal fluctuations in atomically thin clean-limit superconductors. *arXiv preprint arXiv:1909.08469* (2019).
49. Maji, K. *et al.* Superconducting cavity-based sensing of band gaps in 2D materials. *Nano Letters* **24**, 4369–4375 (2024).
50. Wang, J. I. *et al.* Hexagonal boron nitride as a low-loss dielectric for superconducting quantum circuits and qubits. *Nature Materials* **21**, 398–403 (2022).

51. Dean, C. R. *et al.* Boron nitride substrates for high-quality graphene electronics. *Nature Nanotechnology* **5**, 722–726 (2010).
52. Sinko, M. R. *et al.* Superconducting contact and quantum interference between two-dimensional van der Waals and three-dimensional conventional superconductors. *Physical Review Materials* **5**, 014001 (2021).
53. Probst, S., Song, F., Bushev, P. A., Ustinov, A. V. & Weides, M. Efficient and robust analysis of complex scattering data under noise in microwave resonators. *Review of Scientific Instruments* **86** (2015).
54. Nayfeh, A. H., Mook, D. T., *et al.* *Nonlinear Oscillations* (John Wiley & Sons, 2008).
55. Lee, J. C., Oliver, W. D., Berggren, K. K. & Orlando, T. Nonlinear resonant behavior of a dispersive readout circuit for a superconducting flux qubit. *Physical Review B—Condensed Matter and Materials Physics* **75**, 144505 (2007).
56. Vijay, R., Devoret, M., Siddiqi, I., *et al.* Invited review article: The Josephson bifurcation amplifier. *Review of Scientific Instruments* **80** (2009).
57. Andersen, C. K. *et al.* Quantum versus classical switching dynamics of driven dissipative Kerr resonators. *Physical Review Applied* **13**, 044017 (2020).
58. Winkel, P. *et al.* Implementation of a transmon qubit using superconducting granular aluminum. *Physical Review X* **10**, 031032 (2020).
59. Weiβl, T. *et al.* Kerr coefficients of plasma resonances in Josephson junction chains. *Physical Review B* **92**, 104508 (2015).
60. Dvir, T. *et al.* Spectroscopy of bulk and few-layer superconducting NbSe₂ with van der Waals tunnel junctions. *Nature Communications* **9**, 598 (2018).
61. Ugeda, M. M. *et al.* Characterization of collective ground states in single-layer NbSe₂. *Nature Physics* **12**, 92–97 (2016).
62. Coumou, P. *et al.* Microwave properties of superconducting atomic-layer deposited TiN films. *IEEE transactions on applied superconductivity* **23**, 7500404–7500404 (2012).
63. Homes, C., Dai, Y., Wen, J., Xu, Z. & Gu, G. FeTe_{0.55}Se_{0.45}: A multiband superconductor in the clean and dirty limit. *Physical Review B* **91**, 144503 (2015).
64. Dai, Y. *et al.* Coexistence of clean-and dirty-limit superconductivity in LiFeAs. *Physical Review B* **93**, 054508 (2016).
65. Pearl, J. Current distribution in superconducting films carrying quantized fluxoids. *Applied Physics Letters* **5**, 65 (1964).
66. Fridman, N. *et al.* Anomalous thickness dependence of the vortex pearl length in few-layer NbSe₂. *Nature Communications* **16**, 2696 (2025).

67. Srivastava, Y. K. *et al.* $\text{YBa}_2\text{Cu}_3\text{O}_7$ as a high-temperature superconductor. *Nature Materials*, 1–8 (2025).
68. Shein, K. *et al.* Fundamental limits of few-layer NbSe_2 microbolometers at terahertz frequencies. *Nano Letters* **24**, 2282–2288 (2024).
69. Wang, J. I.-J. *et al.* Coherent control of a hybrid superconducting circuit made with graphene-based van der Waals heterostructures. *Nature Nanotechnology* **14**, 120–125 (2019).
70. Wang, L. *et al.* One-dimensional electrical contact to a two-dimensional material. *Science* **342**, 614–617 (2013).
71. Pizzocchero, F. *et al.* The hot pick-up technique for batch assembly of van der Waals heterostructures. *Nature Communications* **7**, 11894 (2016).
72. Grünhaupt, L. *et al.* An argon ion beam milling process for native AlOx layers enabling coherent superconducting contacts. *Applied Physics Letters* **111** (2017).
73. Sanna, A. *et al.* Real-space anisotropy of the superconducting gap in the charge-density wave material 2H-NbSe_2 . *npj Quantum Materials* **7**, 6 (2022).
74. Yokoi, M. *et al.* Negative resistance state in superconducting NbSe_2 induced by surface acoustic waves. *Science Advances* **6**, eaba1377 (2020).
75. Baity, P. G. *et al.* Circle fit optimization for resonator quality factor measurements: Point redistribution for maximal accuracy. *Physical Review Research* **6**, 013329 (2024).
76. Reagor, M. J. *Superconducting cavities for circuit quantum electrodynamics* (Yale University, 2016).
77. Yurke, B., Buks, E., *et al.* Performance of cavity-parametric amplifiers, employing Kerr nonlinearites, in the presence of two-photon loss. *Journal of Lightwave Technology* **24**, 5054–5066 (2006).
78. Norris, G. J. *et al.* Improved parameter targeting in 3D-integrated superconducting circuits through a polymer spacer process. *EPJ Quantum Technology* **11**, 5 (2024).
79. Pozar, D. M. *Microwave Engineering* (John wiley & sons, 2011).
80. Parks, R. & Tinkham, M. *Superconductivity Vols. 1, 2* 1970.
81. Orlando, T. P. & Delin, K. A. *Foundations of Applied Superconductivity* (Addison-Wesley, 1991).
82. Orlando, T., McNiff Jr, E., Foner, S. & Beasley, M. Critical fields, Pauli paramagnetic limiting, and material parameters of Nb_3Sn and V_3Si . *Physical Review B* **19**, 4545 (1979).
83. Xi, X. *et al.* Strongly enhanced charge-density-wave order in monolayer NbSe_2 . *Nature Nanotechnology* **10**, 765–769 (2015).
84. He, R. *et al.* Interlayer breathing and shear modes in NbSe_2 atomic layers. *2D Materials* **3**, 031008 (2016).
85. Lui, C. H., Ye, Z., Keiser, C., Xiao, X., He, R., *et al.* Temperature-activated layer-breathing vibrations in few-layer graphene. *Nano Letters* **14**, 4615–4621 (2014).

Data availability

The data that support the findings of this study are available from the corresponding author upon reasonable request and with the cognizance of our US Government sponsors, who funded the work.

Supplementary Information

Contents

1	Device Assembly and Fabrication	23
2	Optimization of the Contact Resistance between hBN encapsulated NbSe₂ and Al	24
3	Measurement Setup	25
4	Resonator Circular Fit	26
5	Non-linearity of the Resonator from the Inductance	26
6	Extraction of Kinetic Inductance from Resonance Frequency	28
7	Kinetic inductance: Clean and Dirty Limits	29
7.1	Clean Limit	29
7.2	Dirty Limit	30
7.3	Full range calculation: from clean to dirty limit	31
8	Pearl Length	32
9	Determination of NbSe₂ Thickness and Layer Number	32
9.1	AFM characterization of hBN-NbSe ₂ -hBN stack	32
9.2	Raman Spectroscopy of thin NbSe ₂ films	32

1 Device Assembly and Fabrication

Aluminum CPW resonators are fabricated from a highly resistive 2-inch Si wafer coated with 250 nm MBE-grown aluminum film. The resonator circuit is patterned via photolithography and wet etched using Transene Aluminum etchant. Afterwards, the 2-inch wafer is diced into 5 mm by 5 mm chips. The bulk crystal of NbSe₂ is grown by HQ Graphene. The mechanical exfoliation and encapsulation of thin NbSe₂ layers with hBN are carried out inside an Argon-filled glove box, maintaining oxygen and water levels below 0.1 ppm. This prevents oxidation of NbSe₂, keeping the devices within the low-disorder regime. The hBN-NbSe₂-hBN heterostructures are transferred on the chip using dry polymer-based techniques [69–71]. After transferring the hBN-NbSe₂-hBN stacks onto the pre-patterned chips, the van der Waals heterostructures are taken out

of the glove box. To process edge-contact, first the stack goes through reactive-ion etching with $O_2/Ar/CHF_3$ to open edges of $NbSe_2$. The samples are immediately loaded into an e-beam evaporator to do in-situ ion-milling to clean the exposed edges. Aluminum is then deposited onto the cleaned $NbSe_2$ edge at a tilt angle of 30° with the substrate rotating at 60 rpm, ensuring uniform coverage [52]. The bridging between the contact aluminum and the pre-fabricated aluminum resonator and ground plane is done by another in-situ ion mill and a normal aluminum deposition [72].

2 Optimization of the Contact Resistance between hBN encapsulated $NbSe_2$ and Al

It is critical to establish a low-resistance, transparent contact (with near-zero contact resistance) between hBN encapsulated $NbSe_2$ and the aluminum electrode for achieving impedance matching and accurate resonant frequency measurements. A low contact resistance (R_c) is required because if it exceeds the characteristic impedance (50Ω for our case), the resonator behaves like a $\lambda/2$ -resonator instead of the desired $\lambda/4$ mode terminated with $NbSe_2$ sample. This happens because the higher resistance causes the end of the resonator to act like an open circuit, disrupting the intended resonant behavior. Additionally, minimizing R_c reduces dissipation and enables high-Q, high-accuracy measurements for characterizing the kinetic inductance and other superconducting properties of $NbSe_2$.

We fabricate a few devices for DC measurement using the above fabrication procedures to confirm a reliable superconducting contact between thin $NbSe_2$ and Al. We vary the ion-milling duration to determine the optimal time needed to remove oxides from the edges of $NbSe_2$. To eliminate the line resistances, we measure the devices in a pseudo-4-probe configuration, Fig. S1a. Below the transitions of both $NbSe_2$ and Al, the total resistance of the device, including the Al- $NbSe_2$ junctions, drops to zero within the noise floor of our measurement ($R_c = 0.01\Omega$) Fig. S1b-c. We present the results of the measurement of DC contact devices to optimize the contact resistance as a function of the ion milling time. The results are summarized in the Table S1. We chose the optimum ion milling time of 105 seconds for our microwave devices presented in the main text. The bulk $NbSe_2$ undergoes a transition into the charge-order phase at $T \sim 33\text{ K}$, and a transition into the superconducting phase at $T \sim 7\text{ K}$ [39, 43, 73]. As the thickness of $NbSe_2$ decreases, the critical temperature (T_c) decreases, as shown in Fig. S1d, our results are consistent with other studies in the literature [38]. All our $NbSe_2$ samples are high-quality crystals with relatively high residual resistance ratios ($R_{300\text{K}}/R_N = 5\text{-}10$) [43], the normal-state sheet resistance (R_s) right above the superconducting transition increases as the thickness of $NbSe_2$ decreases; the values are summarized in Table S1. Figure S1e-f

Ion-milling time (sec)	R_c ($\Omega/\mu\text{m}$)	R_s (Ω/sq)	T_c (K)	d (nm)
120	0.01	N/A	N/A	10
105	0.01	31	5.5	6
90	0.01	19	7	8
90	0.02	N/A	N/A	4
80	1.80	60	4.8	4
75	0.02,2	29	5.5	6
60	0.02	45	4.9	5

Table S1: **Summary of DC samples for contact resistance characterization.** The in-situ ion-milling time and the thickness of NbSe_2 both have been varied to characterize the contact resistance between NbSe_2 edge and aluminum interface.

shows four-terminal transport characterization of one of the devices ($d = 8 \text{ nm}$) using current biasing. The differential resistance was measured by applying a small AC excitation current (1 nA) superimposed on a DC bias current and detecting the AC voltage (dV) between two electrodes. The critical current of the NbSe_2 sample is of order 0.4 mA, which is consistent with the previous study [68, 74].

3 Measurement Setup

Figure S2 shows the wiring diagram of the measurement setup used for this work. To send the microwave signals down to the package, we use semi-rigid coaxial cables with low thermal conductivity and low-loss superconducting niobium-titanium (NbTi) cables for the readout. Within our readout input lines, we have integrated attenuation mechanisms: a 20 dB attenuator at 4 K, a 20 dB attenuator at the still plate, and a 30 dB attenuator at the mixing chamber stage. The output signals pass through a 2 GHz high-pass filter and a 12 GHz low-pass filter. We have a Josephson traveling-wave parametric amplifier (TWPA) in our read-out chain, and the TWPA pump tone is combined with the readout signal using a directional coupler, and the signal undergoes a final amplification stage employing a low-noise high-electron-mobility transistor (HEMT) amplifier positioned at the 4 K stage and a room temperature amplifier. DC lines connected to the device are filtered at 4 K with an RC π -filter and an RF+RC filter with a cut-off frequency of 50 kHz at the mixing chamber stage. The control electronics used in this experiment are listed in the Table S2.

Component	Manufacturer	Model
Dilution Refrigerator	Bluefors	XLD1000
VNA	Keysight	N5232A
DC Source	QDevil	QDAC
Lock-in Amplifier	Stanford Research Systems	SR830
Multimeter	Keithley	2010

Table S2: **Summary of control electronics.** Specifications of the control equipment used in the experiment, with their manufacturer and Model numbers.

4 Resonator Circular Fit

For notch-type geometry, where the resonator is coupled to a transmission line, the frequency-dependent transmission S_{21} is given by [53, 75]:

$$S_{21}^{notch}(f) = ae^{i\alpha} e^{-2\pi if\tau} \left[1 - \frac{\left(\frac{Q_L}{|Q_c|}\right) e^{i\phi}}{1 + 2iQ_L \left(\frac{f}{f_r} - 1\right)} \right] \quad (3)$$

where f is the signal frequency, f_r is the resonance frequency, Q_L is the loaded quality factor, Q_c is the coupling quality factor, and ϕ corresponds to the phase shift of resonance due to the impedance mismatch with the transmission line. The prefactor ($ae^{i\alpha}$) includes the overall gain and phase delay of the transmission line, including all the attenuation and amplification. Additionally, τ denotes the propagation time in the transmission line, which introduces a phase shift proportional to the frequency f . Figure S3 shows the raw data (blue) and the Lorentzian fit using Eq. 3 (red) of the spectator resonator in the single-photon limit. We extract the values of the loaded quality factor (Q_L) and the coupling quality factor (Q_c) from the fit. The internal loss determines the intrinsic quality (Q_i) of the resonator extracted from: $\frac{1}{Q_L} = \frac{1}{Q_i} + \frac{1}{Q_c}$. The fitted internal quality factors (Q_i) of six different $\lambda/4$ -resonators are plotted in Fig. S4c.

5 Non-linearity of the Resonator from the Inductance

We observe the resonant frequency shift in the NbSe_2 -terminated resonator at higher microwave power (Fig. 3, main text), while the Al-terminated resonator does not show this behavior (Fig. S4b). The resonant frequency shift with increasing photon number in the resonator is described by the Kerr Hamiltonian [54, 76, 77]

$$H = \hbar\omega_r a^\dagger a + \frac{\hbar}{2} K a^\dagger a^\dagger a a \quad (4)$$

where \hbar is the reduced Planck constant, a and a^\dagger are the creation and the annihilation operators, ω_r is the resonant frequency, and K is the Kerr constant, which is a measure of the strength of the nonlinearity in the system. The Kerr nonlinearity shifts the resonance frequency and is proportional to the resonator photon number. In addition to the power-dependent frequency shift, we observe a broadening of the internal linewidth as the number of photons in the cavity increases. The Kerr coefficient of NbSe_2 is determined by analyzing the relationship between the resonance frequency shift (Δf) and the resonator photon number (n_r) in the resonator. We calculate the photon number in the resonator as a function of the applied power using the following formula [78],

$$n_r = \frac{2\kappa P_{\text{rf}}}{\hbar\omega_r(\kappa + \gamma)^2} \quad (5)$$

Here, κ represents the coupling rate to the feedline, P_{rf} is the power applied at the resonator input, and γ is the internal loss rate.

Expanding the current-dependent kinetic inductance relation of Eq. 1 (main text), the quartic energy contribution is expressed as

$$U_m = \frac{1}{2} L_k \frac{I_{\text{DC}}^4}{I^{*2}} \quad (6)$$

Here, I^* sets the scale for the non-linearity of the film. Applying circuit quantization, the current operator can be expanded in terms of ladder operators as $\hat{I}_{\text{DC}} = I_{\text{zpf}}(a + a^*)$ where $I_{\text{zpf}} = \sqrt{\frac{\hbar\omega_r}{2L_0}}$ is the zero-point current fluctuation of the mode and L_0 is the total inductance of the resonator mode. We obtain the quantized nonlinear energy term of Eq. 6 as

$$\hat{U}_m = \frac{1}{2} L_k \frac{I_{\text{zpf}}^4}{I^{*2}} (a + a^*)^4 \quad (7)$$

The Kerr nonlinearity arises from the term proportional to a^*a^*aa in the quartic expansion, and the resulting Kerr coefficient (K) is

$$K = \frac{6L_k I_{\text{zpf}}^4}{\hbar I^{*2}} = \frac{3\hbar\omega_r^2}{2L_0^2} \cdot \frac{L_k}{I^{*2}} \quad (8)$$

For device D6 (shown in Fig. 3 of the main text), we calculate the Kerr coefficient to be $K/2\pi = -3.8$ Hz/photon using Eq. 8, which is in good agreement with the value ($K/2\pi = -1.7$) extracted from the power-dependent frequency shift. The calculation uses $f_{\text{r,Al-NbSe}_2} = 4.79$ GHz, $L_0 = L_g + L_k = 2.627$ nH,

and $I^* = 0.4 \text{ mA}$.

6 Extraction of Kinetic Inductance from Resonance Frequency

To extract the kinetic inductance (L_k) of NbSe_2 , we employ a comparative model using $\lambda/4$ -resonators terminated with aluminum and NbSe_2 . For the aluminum-terminated resonator with a length of l and a resonant frequency of $f_{r,Al}$, the input impedance Z_{Al} is expressed as [79]

$$Z_{Al,in} = Z_0 \tanh(\alpha + i\beta)l \quad (9)$$

where, Z_0 is the characteristic impedance which is 50Ω in our work, α and β are the attenuation constant and phase constant respectively. For a lossless line, the attenuation constant α is zero, and $\beta(f)$ becomes

$$\beta(f) = \frac{2\pi f_{r,Al} \sqrt{\epsilon_{eff}}}{c} \quad (10)$$

where ϵ_{eff} is the effective permittivity of the substrate (Si), and c is the speed of light in vacuum. Assuming a low-loss transmission line, we take $\alpha = 0$, so that the input impedance simplifies to $Z_{Al,in} = iZ_0 \tan(\beta l)$. On resonance, $\beta l = \pi/2$, which yields the resonant frequency of the Al-terminated resonator $f_{r,Al} = \frac{c}{4l\sqrt{\epsilon_{eff}}}$.

For the $\lambda/4$ -resonator terminated by NbSe_2 , the kinetic inductance (L_k) contributes an additional frequency-dependent term in the impedance, which is modeled as,

$$Z_{Al-\text{NbSe}_2,in} = Z_0 \frac{i\omega_{r,Al-\text{NbSe}_2} L_k + Z_0 \tanh(i\beta l)}{Z_0 + i\omega_{r,Al-\text{NbSe}_2} L_k \tanh(i\beta l)} \quad (11)$$

The physical length l of the resonator is determined from the aluminum reference resonator using Eq. 9, assuming identical geometry and effective permittivity. On resonance, the impedance of a $\lambda/4$ -resonator diverges; for the NbSe_2 -terminated case, Eq. 11 reduces to

$$\tan\left(\frac{\omega_{r,Al-\text{NbSe}_2} \sqrt{\epsilon_{eff}}}{c} l\right) = \frac{Z_0}{\omega_{r,Al-\text{NbSe}_2} L_k} \quad (12)$$

We extract the kinetic inductance L_k of NbSe_2 from Eq. 12, where the resonant frequency of NbSe_2 -terminated resonator is in the linear regime (in the single-photon limit).

7 Kinetic inductance: Clean and Dirty Limits

The purity of a superconductor is characterized by the ratio of the mean free path (l_{MFP}) of the Cooper pairs to the BCS coherence length (ξ_0). The mean free path (l_{MFP}) is defined as $l_{\text{MFP}} = \tau v_F$ with τ representing the time interval between collisions in the normal state of the superconductor and v_F denoting the Fermi velocity [32]. The superconductor is in the dirty metal limit if the mean free path (l_{MFP}) is much shorter than the BCS coherence length (ξ_0), and in the clean limit if l_{MFP} is much longer than ξ_0 [80]. To obtain kinetic inductance for both the dirty and clean limit, two pieces of information are required: (1) the generalized first London equation for a superconductor relating current density and electric field, and (2) an expression characterizing the penetration depth (specifically in the dirty/clean limit). The first London equation establishes a direct relation between the supercurrent density (\vec{J}) and the electric field (\vec{E}),

$$\frac{\partial \vec{J}}{\partial t} = \frac{1}{\mu_0 \lambda^2} \vec{E} \quad (13)$$

where λ is the penetration depth and μ_0 is the permeability of free space. When combined with Maxwell's equations, the London formalism further predicts that magnetic fields decay exponentially inside a superconductor, with the characteristic length λ . With a sinusoidal drive of frequency ω , Eq. 13 gives

$$i\omega (\mu_0 \lambda^2) J = E \quad (14a)$$

$$i\omega \left(\mu_0 \lambda^2 \frac{l}{A} \right) I = V \quad (14b)$$

Equation 14b follows from the substitutions $V = El$ and $I = JA$, and the prefactor in the parentheses represents the kinetic inductance.

$$L_k = \mu_0 \lambda^2 \frac{l}{A} \quad (15)$$

Equation 15 depends on the phenomenological parameter λ , which needs to be evaluated in both clean and dirty limits.

7.1 Clean Limit

In the clean limit, where the mean free path of the superconducting carriers is much longer than the coherence length, scattering events can be neglected. In this case, the dynamics of the supercurrent are determined

solely by the acceleration of Cooper pairs under the applied electric field. This leads to the relation

$$\frac{d}{dt}(m_{\text{eff}}\vec{v}) = \frac{d}{dt}\left(\frac{m_{\text{eff}}}{n_0e^2}\vec{J}\right) = \vec{E} \quad (16)$$

Here, n_0 is the carrier density and m_{eff} is the effective mass of the supercurrent carriers. Equation 16 allows us to identify the penetration depth (λ_{clean}) and kinetic inductance ($L_{k,\text{clean}}$) in the clean limit as,

$$\mu_0\lambda_{\text{clean}}^2 = \frac{m_{\text{eff}}}{n_0e^2} \quad (17)$$

$$L_{k,\text{clean}} = \frac{m_{\text{eff}}}{n_0e^2} \left(\frac{l}{A}\right) \quad (18)$$

This penetration depth is known as the London penetration depth ($\lambda_{\text{clean}} = \lambda_L$).

7.2 Dirty Limit

In the dirty limit, impurity scattering shortens the mean free path of the carriers, which weakens superfluid screening and causes the magnetic field to penetrate deeper, leading to an enhanced penetration depth given by [32, 81],

$$\lambda_{\text{dirty}} \approx \mu_0\lambda_L \left(\frac{\xi_0}{l_{\text{MFP}}}\right)^{1/2} \quad (19)$$

where ξ_0 is the BCS coherence length at zero temperature ($\xi_0 = \frac{\hbar v_F}{\pi\Delta_0} = \xi_{\text{clean}}$) and the coherence length in the dirty limit becomes,

$$\xi_{\text{dirty}} \approx \xi_0 \left(\frac{l_{\text{MFP}}}{\xi_0}\right)^{1/2} = (\xi_0 l_{\text{MFP}})^{1/2} \quad (20)$$

Plugging the expression of λ_{dirty} into the general expression for L_k in Eq. 15, we get

$$L_{k,\text{dirty}} = \mu_0\lambda_{\text{dirty}}^2 \frac{l}{A} = \mu_0\lambda_L^2 \left(\frac{\xi_0}{l_{\text{MFP}}}\right) \frac{l}{A} \quad (21)$$

Now, using the expression of the BCS coherence length ($\xi_0 = \hbar v_F/\pi\Delta_0$) and London penetration depth (λ_L), we obtain

$$L_{k,\text{dirty}} = \frac{m_{\text{eff}}}{n_0e^2} \frac{\hbar v_F}{\pi\Delta_0} \frac{l}{l_{\text{MFP}} A} \quad (22)$$

Equation 22 can be further simplified by substituting the expressions for mean free path ($l_{\text{MFP}} = v_F\tau$) and resistivity ($\rho_s = 1/\sigma$).

$$L_{k,\text{dirty}} = \rho_s \frac{\hbar}{\pi\Delta_0} \frac{l}{A} = R_s \frac{\hbar}{\pi\Delta_0} \frac{l}{w} \quad (23)$$

where R_s is the normal-state sheet resistance of a current-carrying superconducting wire of length l , width w , and film thickness d . The BCS superconducting gap is approximated to $\Delta_0 \approx 1.764k_B T_c$ for $T \ll T_c$ with T_c the critical temperature and Eq. 23 becomes

$$L_{k,sq,dirty} = \frac{\hbar}{1.764k_B} \frac{R_s}{T_c} \quad (24)$$

Layers	$L_{k,sq}$ (pH/sq)	T_c (K)	R_s (Ω /sq)	R_s/T_c (Ω/K)	$L_{k,sq}/L_{k,sq,clean}$
1	1195	3.5 [38]	240 [38]	68.57	14.95
4	282	4.8	60	12.5	3.53
6	191	5.5	29	5.27	2.39
7	143	6.0	25	4.17	1.79
8	135	7	19	2.71	1.79
8	135	6.3 [39]	14 [39]	2.22	1.75
10	56	7.0 [38]	10 [38]	1.43	0.71

Table S3: **Kinetic inductance of NbSe_2 from clean to dirty limit**

7.3 Full range calculation: from clean to dirty limit

We can calculate the kinetic inductance for arbitrary ξ_0/l_{MFP} (where the ratio of ξ_0/l_{MFP} is of the order of 1). The Ginzburg-Landau theory gives a penetration depth of the form which can be well approximated by (Eq. 3.123b in [32] and the appendix in [82]):

$$\lambda = \lambda_L \left(1 + a \frac{\xi_0}{l_{MFP}} \right)^{1/2} \quad (25a)$$

$$L_k = \mu_0 \lambda_L^2 \left(1 + a \frac{\xi_0}{l_{MFP}} \right) \left(\frac{l}{A} \right) \quad (25b)$$

$$L_{k,sq} = \mu_0 \frac{\lambda_L^2}{d} + \mu_0 \frac{\lambda_L^2}{d} \left(a \frac{\xi_0}{l_{MFP}} \right) \quad (25c)$$

The factor a in Eq. 25a-c is the order of unity ($a = 0.75$), but we have set a to be unity in the main text for simplicity. Equation 25c indicates that the kinetic inductance per square is the sum of the clean and dirty limit results. We can extract the ratio of coherence length to mean free path ($\frac{\xi_0}{l_{MFP}}$) from the above expression.

$$\frac{\xi_0}{l_{MFP}} = \frac{L_{k,sq}}{L_{k,sq,clean}} - 1 \quad (26)$$

Figure S5 shows the clean- and dirty-limit contributions to the measured sheet kinetic inductance $L_{k,sq}$ of NbSe_2 samples, highlighting the $1/d$ dependence of the clean-limit term in thicker samples and the dominant dirty-limit contributions in thinner samples.

Figure S5 plots results from the second expression in Eq. 2 which is of the form $L_{k,\text{sq}} = A/d + (\hbar 1.764k_B)R_s/T_c$. Figure S5a plots $L_{k,\text{sq}} \times d$ versus ρ/T_c where $\rho = R_s d$. The y-intercept of Fig. S5a is used to get an estimate of A . Figure S5b uses this value of A to plot, $L_{k,\text{sq}} - A/d$ versus R_s/T_c , where the y axis now shows the contribution to $L_{k,\text{sq}}$ from the dirty limit. Given that A/d is about 70 pH for the 10 layer sample, the values for the thicker samples have smaller contributions from the dirty limit term and are thus mostly in the clean limit. The samples for high sheet resistance are dominated by the dirty limit contribution.

8 Pearl Length

In superconducting films where the thickness d is much smaller than the penetration depth λ_L ($d \ll \lambda$), magnetic fields are weakly screened in the transverse direction and instead spread laterally over long distances. This lateral field penetration is characterized by the Pearl length, defined as

$$\Lambda = \frac{2\lambda}{d} \quad (27)$$

The Pearl lengths of all the devices in this work are estimated using Eq. 27, where the penetration depth of NbSe_2 is 230 nm.

9 Determination of NbSe_2 Thickness and Layer Number

9.1 AFM characterization of hBN- NbSe_2 -hBN stack

Atomic force microscopy (AFM) is a high-resolution imaging technique used in this work to characterize the surface topography and height of hBN- NbSe_2 -hBN stacks. The thickness of hBN encapsulated NbSe_2 is determined by tapping-mode AFM, illustrated in Fig. S8. The AFM measurement tends to overestimate the actual thickness of NbSe_2 due to the presence of the top hBN encapsulation. In this work, the effective NbSe_2 thickness is slightly smaller, as confirmed by the shear mode in the low-frequency Raman spectrum.

9.2 Raman Spectroscopy of thin NbSe_2 films

The number of layers in our samples was determined by the shear mode frequency of Raman spectroscopy [83, 84]. The Raman data were collected using a Horiba LabRAM Evolution system in the XY channel at room temperature. A 50x objective (Mitutoyo MY50X-825) was employed to direct and collect light in the backscattering geometry with a 532 nm wavelength. Data were captured using a liquid nitrogen-cooled CCD,

maintained at -133°C. The incident laser power on the sample was estimated to be below 4 mW. Figure S7b shows that the low-frequency mode observed in the Raman spectra corresponds to interlayer shear modes. In all spectra, shear modes are analyzed using Lorentzian peak fitting after subtracting the background. The shear mode peak in Raman spectra originates from interlayer shearing and is absent in the monolayer sample. The frequency of the shear modes (ω_s) decreases with decreasing layer number (N), reflecting a reduced effective interlayer spring constant. The relationship can be described as $\omega_s = \omega_{s,\text{Bulk}} \cos(\frac{\pi}{2N})$ with a bulk shear mode frequency $\omega_{s,\text{Bulk}} = 29.39 \text{ cm}^{-1}$ [84, 85]. The AFM-measured thicknesses of the NbSe₂ flakes are consistent with the layer numbers determined from the shear mode frequency (1 layer = 1 nm) for all samples except for the thinnest device D1 (see main text table). For D1, the AFM measurement indicates a thickness of 2 nm, while Raman spectroscopy only shows a weak feature at the frequency 19.04 cm⁻¹ rather than a well-defined Lorentzian peak (Fig S7b). This corresponds to a layer number less than 2, with a fitted value of $N = 1.5$ (Fig. S7a). We use this Raman-derived value (1.5 nm) in the analysis presented in Fig. 4a.

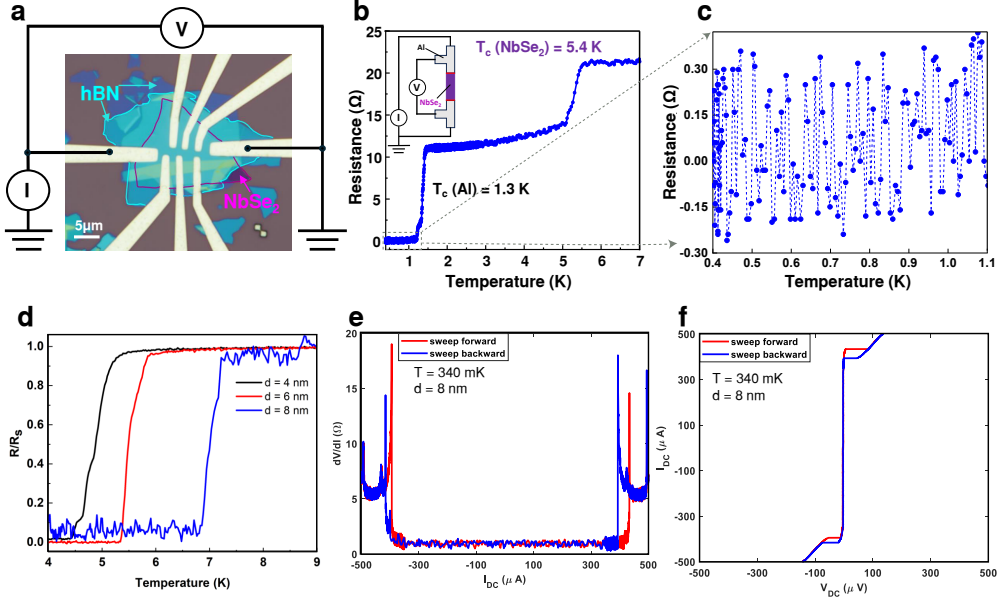


Figure S1: **Al and NbSe_2 interface characterization and DC characteristics of NbSe_2 .** **a**, Optical micrograph of a pseudo-4-probe DC device where hBN flakes fully encapsulate NbSe_2 flake, the current is applied between two terminals, and voltage is measured across those two terminals without taking into account the line resistance of the measurement setup. **b**, Resistance(T) for Al- NbSe_2 -Al device showing the superconducting transition of NbSe_2 ($d = 6$ nm) at 5.4 K and the superconducting transition of Al at 1.3 K. Inset represents the 4-pt measurement setup for measuring the contact resistances of the Al/ NbSe_2 interfaces. **c**, Total Resistance of the device below Al transition, which has dropped to zero within the noise floor of the measurement. **d**, Temperature dependence of the resistance for devices with NbSe_2 thicknesses of 4 nm, 6 nm, and 8 nm. To extract the T_c , we use the mean-field definition of T_c , which corresponds to half of the normal state resistance. **e**, Differential resistance (dV/dI) measurement for the $d = 8$ nm thick NbSe_2 of 4-point DC measurement. The plot shows the critical current $400 \mu\text{A}$ for that device. **f**, Current-voltage (I-V) relation on the same device.

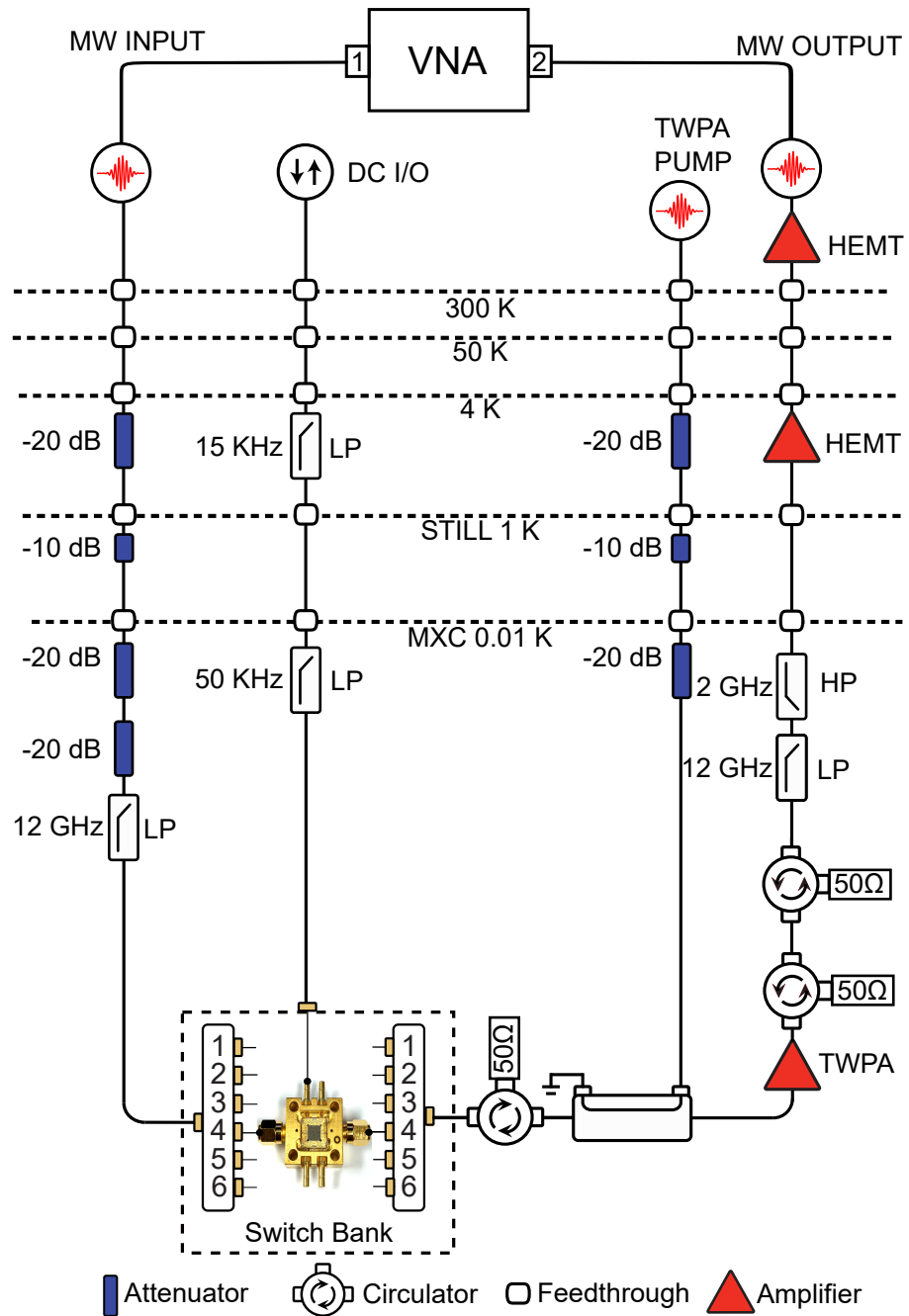


Figure S2: **Measurement setup.** Wiring diagram of the microwave and DC setup to the device.

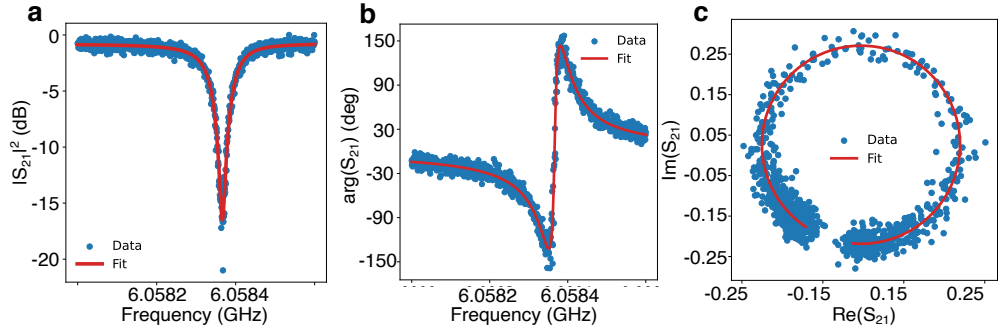


Figure S3: **Raw data (blue) and Lorentzian fit (red) of Al ‘spectator’ $\lambda/4$ -resonator.** **a-b** Magnitude and phase response of S_{21} signal as a function of frequency at the single photon limit. The equation 3 function is used to fit the complex response. **c**, The imaginary part of S_{21} is plotted versus its real part, where the circle diameter corresponds to $Q_L/Q_c = \frac{Q_i/Q_c}{(Q_i/Q_c)+1}$, which determines the contributions of coupling and internal losses of the resonator. The fitted resonance frequency is 6.0583 GHz, with an internal quality factor, Q_i is 5.985×10^6 , and a coupling quality factor, Q_c is 10^5 .

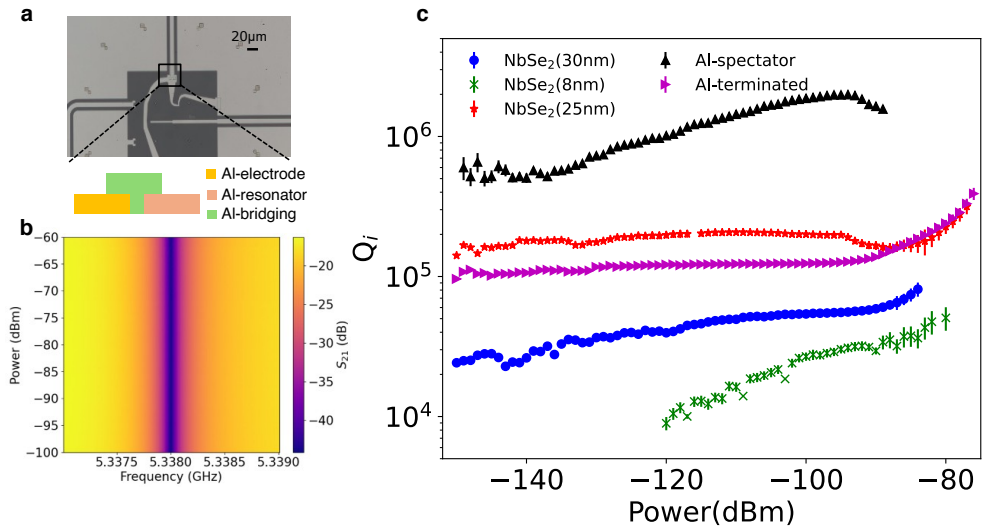


Figure S4: **Measurements of $\lambda/4$ resonator.** **a**, Optical image of Al-terminated resonator of similar geometry used in Fig 3 (main text). Here, two different Al layers (one MBE grown (orange) and another e-beam evaporated (yellow)) are made contact through an aluminum bridging step (green). The bridging step is performed by doing in-situ ion-milling to remove the native oxide layer and evaporate another layer of aluminum. **b**, Magnitude response of Al-shunted resonator with varying the input microwave power from -100 dBm to -60 dBm. The resonant frequency has a very negligible change, showing a small contribution of kinetic inductance from aluminum. **c**, Comparison of quality factors across different types of $\lambda/4$ resonators discussed in this work.

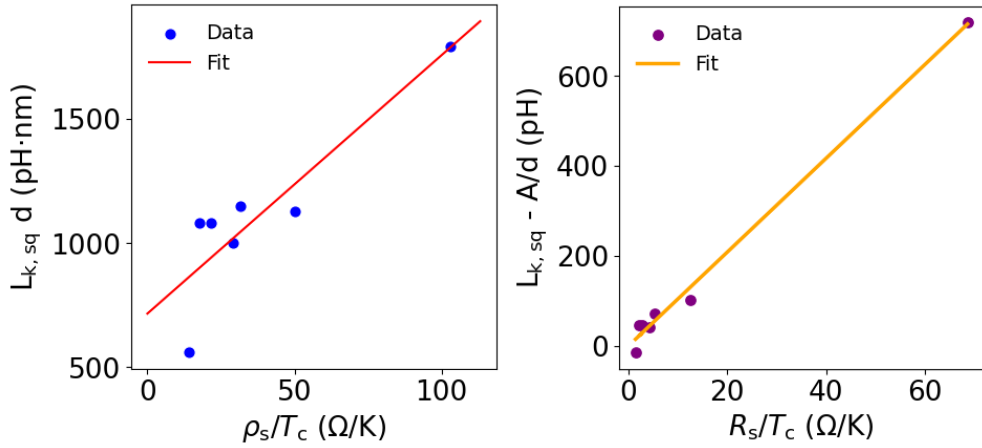


Figure S5: **a**, The linear relationship of $L_{k,\text{sq}} \times d$ with ρ_s/T_c where the intercept of the y-axis sets the value of the fitting parameter $A = \frac{m_{eff}}{n_0 e^2}$. **b**, $L_{k,\text{sq}} - \frac{A}{d}$ is plotted as a function of R_s/T_c , where the linear fit shows the dirty limit contribution for the thinner samples of NbSe_2 .

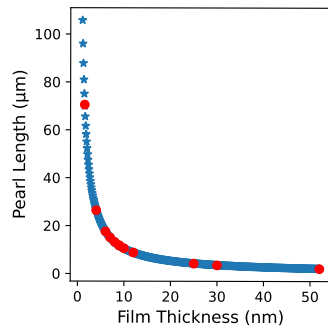


Figure S6: **Pearl length estimation (blue)** of NbSe_2 of different thicknesses with consideration of $\lambda_L = 230$ nm. The NbSe_2 samples of this work are identified in red circles.

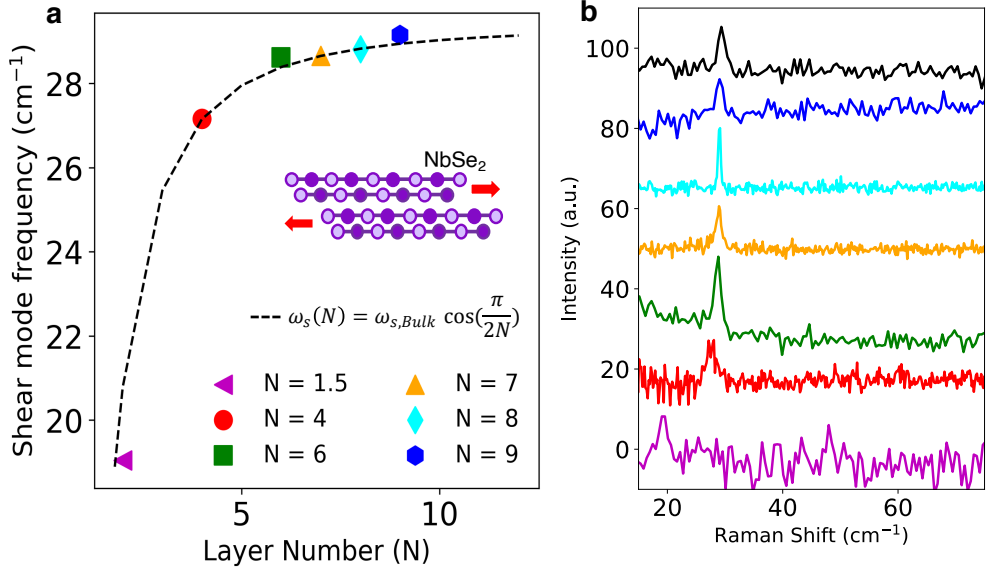


Figure S7: **Low-frequency Raman spectroscopy on different layers of NbSe_2 samples at room temperature under vacuum for the perpendicular polarization configuration.** **a**, Plot of shear mode frequency versus layer numbers of NbSe_2 . The dotted blue line shows the $\omega_s = \omega_{s,Bulk} \cos(\frac{\pi}{2N})$ relation with $\omega_{s,Bulk} = 29.39 \text{ cm}^{-1}$. **b**, Low-frequency Raman spectra of NbSe_2 with layer number $N = 4 - 8$ and bulk NbSe_2 . For clarity, the spectra are vertically displaced.

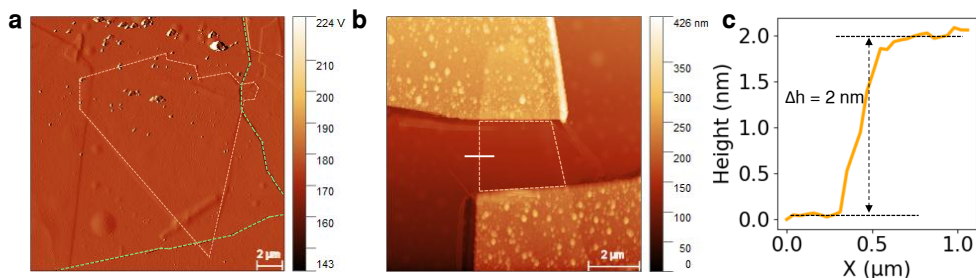


Figure S8: **AFM topographic image of hBN encapsulated NbSe_2 devices.** **a**, Amplitude topography of the NbSe_2 flake following the assembly of the hBN- NbSe_2 -hBN heterostructures (hBN-green and NbSe_2 -orange). **b**, Height profile along the indicated path (white line) to determine the thickness of NbSe_2 .